International Forum on Aeroelasticity and Structural Dynamics
IFASD 2022
13-17 June 2022, Madrid, Spain

FAST FULL POTENTIAL BASED AEROSTRUCTURAL OPTIMIZATION CALCULATIONS FOR PRELIMINARY AIRCRAFT DESIGN

Adrien Crovato[1], Romain Boman[1], Vincent E. Terrapon[1], Grigorios Dimitriadis[1], Alex P. Prado[2], Pedro H. Cabral[2]

[1]University of Liège
Liège, Belgium
{a.crovato, r.boman, vincent.terrrapon, gdimitriadis}@uliege.be

[2]Embraer S.A.
Sao José dos Campos, Brazil
{alex.prado, pedro.cabral}@embraer.com.br

Keywords: Discrete adjoint, Transonic flows, Full potential, Aerostructural optimization, Preliminary aircraft design

Abstract: In order to reduce aircraft fuel consumption and to improve the reliability of the design process, multi-disciplinary optimization is nowadays carried out during the preliminary design stage. These optimization calculations must model the aeroelastic behavior of the aircraft in order to be effective and to take full advantage of composite materials. Since many design variables are involved during the early stages, the optimization problem is usually solved using the adjoint method. Moreover, the fluid model and the associated numerical simulation method must be selected with care, as they are the main contributors to the overall computational cost. In the present work, an open-source full potential solver with discrete adjoint capability is integrated in a multi-disciplinary optimization framework. Aerodynamic and aerostructural optimization calculations are subsequently carried out on typical benchmark cases to illustrate the methodology. Overall, the results show that the adjoint nonlinear potential formulation yields optimized wing shapes and structures at very low computational cost. The next steps consist in improving the problem formulation, by considering full aircraft configurations along with more realistic design variables, constraints and objective functions, and in improving the aerodynamic model by including viscous effects.

1 INTRODUCTION

For the air transport sector to remain economically competitive and to decrease its environmental impact, aircraft fuel consumption must continuously be reduced. To this end, aerodynamic shape optimization is usually performed in conjunction with aeroelastic tailoring [1]. Such an aerostructural optimization process enables the design of light wings with efficient shapes, exploiting the orthotropic mechanical properties of new composite materials, thus guaranteeing good aerodynamic performance and the ability to withstand the aerodynamic loads and the aeroelastic instabilities. The formulation of modern aircraft optimization problems usually involves a few functionals, like the fuel burn and the failure index of the material, and thousands of design variables, such as the wing shape and structural parameters. Moreover, the baseline design is already quite close to the optimal solution, hence not requiring a full exploration of the design space [2, 3]. Consequently, gradient-based optimization is usually employed,

whereby the gradients are computed using the adjoint method [4, 5], as using other methods such as finite-differences would lead to a prohibitive computational cost [6–8]. Despite the recent advances in high-fidelity multidisciplinary optimization, and the ever-increasing available computational power, low-fidelity linear aerodynamic modeling methodologies are still widely used in industry so as to decrease the computational cost [9]. This is particularly the case during preliminary aircraft design, where aerostructural optimization is introduced early to make the design process more robust by directly considering complex fluid-structure interactions, hence helping to prevent future failures resulting from unaccounted aeroelastic behaviors. However, linear models are not accurate in the transonic regime, where modern transport aircraft fly, since nonlinear compressible effects become important and cannot be neglected. A viable trade-off between accuracy and computational cost can be achieved by resorting to the full potential equation [10, 11]. The goal of the present work is to carry out aerodynamic shape and aerostructural optimization calculations on benchmark wings, similar to those performed during preliminary aircraft design, in order to demonstrate the effectiveness and the computational efficiency of the full potential discrete adjoint formulation implemented in the open-source finite element code `DART` [12].

The present work is organized as follows. In section 2, the aerostructural optimization framework and its associated numerical tools are briefly described. Results are then presented in chapter 3. Finally, the last section summarizes and concludes the article, and suggests research directions for future work.

2 METHODOLOGY

2.1 Formulation of the optimization problem

In the present work, the aerostructural optimization problem is formulated using the three-fields formulation, initially developed by Farhat et al. [13] and later improved by Maute et al. [14]. This formulation is required when nonlinear aerodynamic models are used and the geometry is subjected to large displacements, such that the contributions of the grid motion cannot be neglected. The problem is formulated as follows,

$$\begin{aligned} \min_{\mathbf{p}} \; & F_{\text{obj}}(\mathbf{u}, \mathbf{v}, \mathbf{x}; \mathbf{p}) \\ \text{s.t.} \; & \mathbf{R}_{\text{u}} = 0 \\ & \mathbf{R}_{\text{v}} = 0 \\ & \mathbf{R}_{\text{x}} = 0 \\ & \mathbf{C}(\mathbf{u}, \mathbf{v}, \mathbf{x}; \mathbf{p}) = 0, \end{aligned} \tag{1}$$

where $\mathbf{u}$ and $\mathbf{v}$ denote the vector of structural and aerodynamic variables, $\mathbf{x}$ is the vector of volume mesh coordinates, $\mathbf{p}$ is the vector of design variables, $\mathbf{R}_{\text{u}}$ and $\mathbf{R}_{\text{v}}$ represent the structural and aerodynamic equations noted in residual form, $\mathbf{R}_{\text{x}}$ is the vector of residuals of the mesh morphing laws, and $F_{\text{obj}}(\mathbf{u}, \mathbf{v}, \mathbf{x}, \mathbf{p})$ is the functional to be minimized under the constraints $\mathbf{C}(\mathbf{u}, \mathbf{v}, \mathbf{x}, \mathbf{p})$. In order to minimize F_{obj}, the augmented Lagrangian $\mathcal{L}$ is first constructed as

$$\mathcal{L} = F_{\text{obj}} + \lambda_{\text{u}}\mathbf{R}_{\text{u}} + \lambda_{\text{v}}\mathbf{R}_{\text{v}} + \lambda_{\text{x}}\mathbf{R}_{\text{x}}, \tag{2}$$

where λ_u, λ_v and λ_x are Lagrange multipliers, and then differentiated such that

$$\delta\mathcal{L} = 0 \Rightarrow \begin{cases} \frac{\partial F_\mathrm{obj}}{\partial \mathbf{u}} + \lambda_\mathrm{u}\frac{\partial \mathbf{R}_\mathrm{u}}{\partial \mathbf{u}} + \lambda_\mathrm{v}\frac{\partial \mathbf{R}_\mathrm{v}}{\partial \mathbf{u}} + \lambda_\mathrm{x}\frac{\partial \mathbf{R}_\mathrm{x}}{\partial \mathbf{u}} = 0 \\ \frac{\partial F_\mathrm{obj}}{\partial \mathbf{v}} + \lambda_\mathrm{u}\frac{\partial \mathbf{R}_\mathrm{u}}{\partial \mathbf{v}} + \lambda_\mathrm{v}\frac{\partial \mathbf{R}_\mathrm{v}}{\partial \mathbf{v}} + \lambda_\mathrm{x}\frac{\partial \mathbf{R}_\mathrm{x}}{\partial \mathbf{v}} = 0 \\ \frac{\partial F_\mathrm{obj}}{\partial \mathbf{x}} + \lambda_\mathrm{u}\frac{\partial \mathbf{R}_\mathrm{u}}{\partial \mathbf{x}} + \lambda_\mathrm{v}\frac{\partial \mathbf{R}_\mathrm{v}}{\partial \mathbf{x}} + \lambda_\mathrm{x}\frac{\partial \mathbf{R}_\mathrm{x}}{\partial \mathbf{x}} = 0 \\ \frac{\partial F_\mathrm{obj}}{\partial \mathbf{p}} + \lambda_\mathrm{u}\frac{\partial \mathbf{R}_\mathrm{u}}{\partial \mathbf{p}} + \lambda_\mathrm{v}\frac{\partial \mathbf{R}_\mathrm{v}}{\partial \mathbf{p}} + \lambda_\mathrm{x}\frac{\partial \mathbf{R}_\mathrm{x}}{\partial \mathbf{p}} = 0 \\ \mathbf{R}_\mathrm{u} = 0 \\ \mathbf{R}_\mathrm{v} = 0 \\ \mathbf{R}_\mathrm{x} = 0 \end{cases} . \tag{3}$$

The fourth equation represents the total gradient of the functional F_obj with respect to the design variables $\mathbf{p}$. It can be computed by first solving the last three nonlinear equations for the variables $\mathbf{u}$, $\mathbf{v}$ and $\mathbf{x}$, then solving the first three linear equations for the Lagrange multipliers, and finally by injecting those variables into the expression of the total gradient. An optimizer can then be used to drive that gradient to zero, hence finding the optimal values of the design variables. Note that the constraints $\mathbf{C}$ are handled separately from the adjoint formulation.

2.2 Numerical tools

The optimization process is solved using `MPHYS` [1], a modular multiphysics simulation package built on top of the `OpenMDAO` framework [15] [2]. `MPHYS` automates the connection of the different software components used in the optimization process and required by `OpenMDAO`, so that high-fidelity aerostructural computations can be carried out easily. The code is open-source and is developed jointly by NASA and the MDO Lab of the University of Michigan. The Sequential Least Squares Programming (SLSQP) method [16] implemented in `scipy` [17] or `pyOptSparse` [18] [3] is used as the optimization driver.

The aerodynamic surface is parametrized using `pyGeo` [19] [4], a set of python tools providing geometry manipulation features. More specifically, `pyGeo` allows to parametrize and constrain a geometry represented by a surface grid, using the free form deformation technique [20]. The geometry can then be deformed according to some design parameters, and `pyGeo` will calculate the sensitivities of the surface deformation with respect to these parameters. The code is open-source and developed by the MDO Lab.

The aerodynamic model is based on the full potential equation and solved using `DART` [12] [5], a finite element code designed to quickly compute inviscid transonic flows. `DART` allows to calculate the aerodynamic loads and to provide the sensitivities of flow functionals using analytic gradients. The volume mesh deformation procedure is based on linear elasticity [21, 22] and is also embedded in `DART`. The code is open-source, written in C++ and interfaced in python, and developed at the University of Liège. The aerodynamic meshes are created using `Gmsh` [23] [6], a three-dimensional unstructured mesh generation software also actively developed at the University of Liège.

[1] `https://github.com/OpenMDAO/mphys`, accessed March 2022.
[2] `https://openmdao.org/`, accessed March 2022.
[3] `https://github.com/mdolab/pyoptsparse`, accessed March 2022.
[4] `https://github.com/mdolab/pygeo`, accessed March 2022.
[5] `https://gitlab.uliege.be/am-dept/dartflo`, accessed March 2022.
[6] `http://gmsh.info`, accessed March 2022.

The structural equations are solved using TACS [24–27] [7], a finite element code dedicated to the analysis of composite structures. TACS computes the deflection of the structural model when it is subjected to external loads, and provides the sensitivities of structural functionals using analytic gradients. The parametrization of the structural elements is also defined in TACS. The code is written in C++ and interfaced in python. It is developed by both the SMDO group at Georgia Tech and the MDO Lab.

Since the structure and the aerodynamic equations are solved on different grids, the relevant data need to be interpolated from one mesh to another. MELD [28] [8] implements such a transfer scheme, and is used to pass the aerodynamic loads to the structural mesh and the structural displacements to the aerodynamic mesh. The code is written in C++ and interfaced in python, and is developed by the SMDO group.

3 RESULTS

3.1 Aerodynamic shape optimization

The first two optimization calculations are carried out on a NACA 0012 airfoil at Mach number $M_\infty = 0.78$ and on the Onera M6 wing [29] [9] at Mach $M_\infty = 0.839$. Although the first problem is two-dimensional, it is formulated and solved in three dimensions since pyGeo only handles 3D geometries. The objective of the optimization is to minimize the drag coefficient C_D by adapting the shapes of the wing. The geometry is embedded in a free-form deformation (FFD) box, as shown in Figure 1(a), whose control points are restricted to move vertically to control the cross-sectional shape of the wing. Three levels of refinement, summarized in Table 1, are used in order to assess the effect of the box discretization on the results. Additionally, the angle of attack of the freestream flow, α, is allowed to change. Furthermore, in the case of the Onera M6, the points of the sections along the wing span, except for the points located at the centerline, can rotate rigidly in order to create a twist. The lift coefficient of the NACA airfoil is constrained to $C_L = 0.40$, and that of the Onera wing to $C_L = 0.30$. The internal volume of the wing is prevented from decreasing in order to emulate the presence of a structural wingbox. The leading edge radius and the trailing edge thickness are constrained to remain constant so that the leading edge cannot sharpen and the trailing edge cannot collapse. Additionally, the upper and lower control points at the wing leading and trailing edges are constrained to move in equal and opposite direction so that they cannot emulate a twist, which would be redundant with the twist design variables [30]. The optimization tolerance is set to a tenth of a drag count. The optimization problems are summarized in Table 2.

Table 1: Number of control points in the chordwise, spanwise and vertical directions used to discretize the FFD box for the NACA 0012 and the Onera M6 cases.

	NACA 0012			Onera M6		
FFD	n_x	n_y	n_z	n_x	n_y	n_z
Coarse	5	2	2	5	3	2
Medium	7	2	2	7	5	2
Fine	9	2	2	9	7	2

[7] https://github.com/smdogroup/tacs, accessed March 2022.

[8] https://github.com/smdogroup/funtofem, accessed March 2022.

[9] https://www.grc.nasa.gov/www/wind/valid/m6wing/m6wing.html, accessed March 2022.

Table 2: Summary of the NACA 0012 and Onera M6 optimization problems.

	NACA 0012		Onera M6		
Objective	Number	Bounds	Number	Bounds	Scaling
Drag coefficient	1	–	1	–	10^2
Design variables					
Angle of attack	1	$[0; 5]^\circ$	1	$[0; 5]^\circ$	10^{-1}
Shape	$n_x \times n_y \times n_z$	$[-2; 2]$ cm	$n_x \times n_y \times n_z$	$[-1; 1]$ cm	10^1
Twist	–	–	$n_y - 1$	$[-5; 5]^\circ$	10^{-1}
Nonlinear constraints					
Lift coefficient	1	$= 0.40$	1	$= 0.30$	1
Wing volume	1	$[100; -]$ %	1	$[100; -]$ %	1
Leading edge radius	2	$[100; -]$ %	10	$[100; -]$ %	1
Trailing edge thickness	2	$[100; -]$ %	10	$[100; -]$ %	1
Linear constraints					
Leading/trailing edge	2	$= 0$ m	$2 \times n_y$	$= 0$ m	1

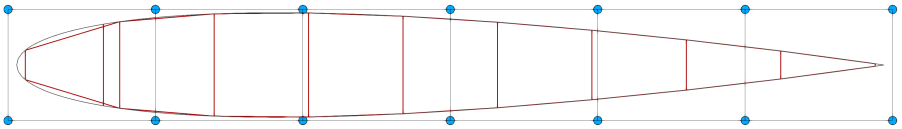

(a) NACA 0012.

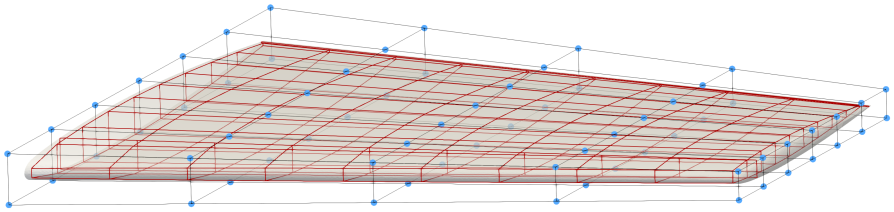

(b) Onera M6.

Figure 1: Optimization setup for the NACA 0012 and the Onera M6 cases. The points controlling the shape design variables are shown in light blue and the shape constraints are displayed in red.

3.1.1 Grid convergence

The aerodynamic computations are performed in domains discretized using tetrahedral elements. Before running the optimization, a grid convergence analysis is first carried out. The results provided in Table 3 indicate that the medium meshes yield converged results, since the difference in aerodynamic coefficients between the coarse and medium grids is much smaller than the difference between the medium and fine grids.

3.1.2 Aerodynamic and pressure coefficients

The angle of attack and integrated aerodynamic coefficients obtained on the baseline and the optimized geometry of the NACA 0012 airfoil and the Onera M6 wing using three levels of refinement of the FFD box are provided in Table 4. Additionally, the pressure coefficient computed on the NACA 0012 is given in Figure 2, and the pressure coefficient computed on four

sections along the span of the Onera M6 wing is given in Figure 3. Note that the second section corresponds to the location of the mean aerodynamic chord. The initial solution on the baseline NACA 0012 was computed at zero angle of attack, as DART could not converge at $C_L = 0.4$ due to the strong shock embedded in the flow. In both cases, the optimization process turns the baseline symmetric airfoils into supercritical ones adapted to the transonic regime. In the NACA case, using the coarse and medium levels of refinement of the FFD box only allows to weaken the shock on the suction side of the airfoil, while using the finest discretization completely removes the shock. In the case of the Onera wing, the shock is not present on any of the optimized geometries, regardless of the level of refinement. Additionally, a negative twist is added on the outboard of the wing. Overall, using more control points to discretize the FFD box allows to further reduce the drag for a given lift. However, fine discretizations also produce undesirable bumps in the solution, creating small-amplitude low-frequency spatial oscillations along the chord. While these bumps are barely noticeable on the solution obtained using the medium FFD, they become pronounced if the fine FFD is used. Furthermore, the fine FFD also creates an airfoil with alternating positive and negative camber at the wing tip of the Onera M6. These nonphysical features may be due to the inviscid nature of the calculations. If the fluid were viscous, a boundary layer would be created, and any bumps would produce more drag, which would drive the optimizer away from such a solution. Viscous effects can be taken into account by complementing the full potential equation by the integral boundary layer equations through a viscous-inviscid interaction method [31]. Such a coupling is currently being developed and implemented in DART [32, 33]. Alternatively, imposing the thickness to change uniformly along the chord might also help alleviate this issue, probably at the cost of obtaining a less optimal solution. It should be mentioned that similar bumps were already noticed in the context of aerodynamic [34] and aerostructural [35] optimization based on the Euler equations, but to a lesser extent. In conclusion, since using fine discretizations of the FFD box only slightly reduces the drag but produces nonphysical features in the optimized solution, it seems desirable to use coarse or medium levels of refinement along with the potential formulation.

3.1.3 Optimization convergence and computational time

The computations were run on a desktop workstation equipped with an AMD 3970X processor rated at 3.7 GHz using a single thread. The number of gradient and functional evaluations, as well as the computational time are given in Table 5. As expected, using finer FFD discretizations amounts to increasing the number of design variables, which decreases the convergence rate and increases the computational cost. Overall, the full potential formulation is very fast and yields optimized aerodynamic shapes in less than a minute for a two-dimensional case, and in less than 30 minutes in three dimensions. The computational cost of the full potential based calculations can be compared to those performed by Lyu et al. [34] using a similar formulation but with the Euler equations. While the present approach only required 10 to 14 gradient evaluations, 112

Table 3: Cell count, aerodynamic coefficients and computational times obtained using three grids for the NACA 0012 at $\alpha = 0°$, $M_\infty = 0.78$ and the Onera M6 at $\alpha = 3.06°$, $M_\infty = 0.839$.

	NACA 0012				Onera M6			
Mesh	N. cells	C_L	C_D	CPU time	N. cells	C_L	C_D	CPU time
Coarse	10 529	0.0382	0.00245	0.4 s	196 080	0.2865	0.01062	0.5 min
Medium	21 639	0.0155	0.00204	1.1 s	477 857	0.2996	0.01126	1.5 min
Fine	39 739	0.0182	0.00189	3.9 s	826 182	0.3013	0.01129	3.5 min

Table 4: Angle of attack and integrated aerodynamic coefficients obtained on the baseline and the optimized geometry of the NACA 0012 airfoil and the Onera M6 wing using three FFD disretizations.

	NACA 0012			Onera M6		
Solution	$\alpha(^\circ)$	C_L	C_D	$\alpha(^\circ)$	C_L	C_D
Initial	0.00	0.016	0.0020	3.06	0.300	0.0113
Coarse FFD	0.19	0.400	0.0018	3.78	0.300	0.0082
Medium FFD	0.00	0.400	0.0015	3.94	0.300	0.0079
Fine FFD	0.00	0.400	0.0013	4.91	0.300	0.0078

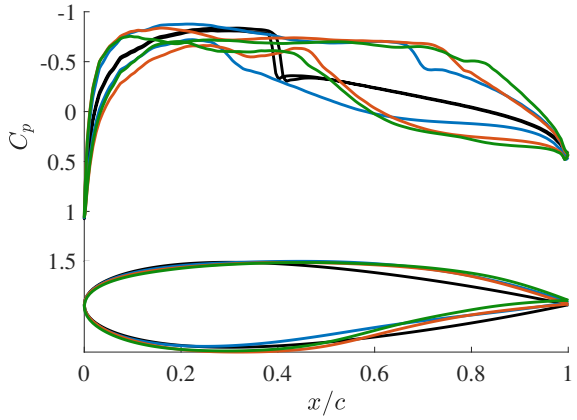

Figure 2: Pressure coefficient computed on the baseline and optimized geometry of the NACA 0012 airfoil at $M_\infty = 0.78$ using three FFD discretizations. Black: baseline, blue: coarse FFD, red: medium FFD, green: fine FFD.

iterations were needed by the Euler calculation for a total computational time of 348 core-hours. Note that the computational time should not be directly compared as the Euler computations were performed on a 2013 supercomputer.

Table 5: Number of gradient and functional evaluations, and computational time required for the NACA 0012 and Onera M6 cases.

	NACA 0012		Onera M6	
FFD	N. grad./func. eval.	Wall-clock time	N. grad./func. eval.	Wall-clock time
Coarse	10/13	31 s	4/11	15 min
Medium	14/30	58 s	8/15	21 min
Fine	13/34	65 s	15/27	34 min

3.2 Aerostructural optimization

The third optimization computation is carried out on the RAE benchmark wing, which is similar to that of a typical regional jet, and whose geometrical and structural parameters are given in Table 6 [10]. The structural model is made of an isotropic material representative of Aluminum 7000

[10]The wing geometry is available at `https://github.com/mdolab/MACH-Aero/tree/master/tutorial/aero/geometry/`. The structural model has been built by the MDO Lab and is available at `https://github.com/OpenMDAO/mphys/tree/main/examples/aerostructural/mach_tutorial_wing/vlm_meld_tacs/`. Links accessed March 2022.

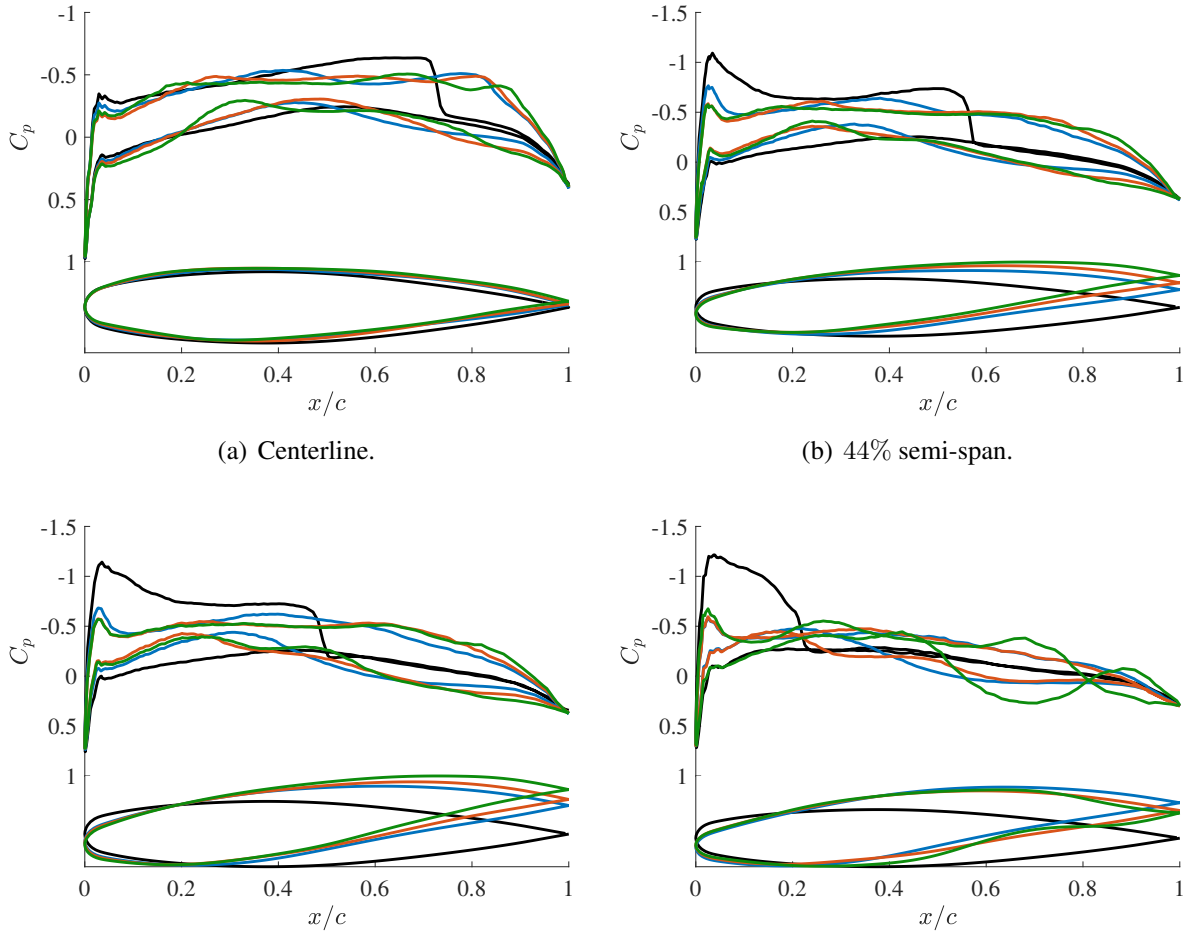

(a) Centerline.

(b) 44% semi-span.

(c) 65% semi-span.

(d) 95% semi-span.

Figure 3: Pressure coefficient computed on the baseline and optimized geometry of the Onera M6 wing at $M_\infty = 0.839$ using three FFD discretizations. Black: baseline, blue: coarse FFD, red: medium FFD, green: fine FFD.

series, and is discretized using second-order shell elements based on the mixed interpolation of tensorial components formulation [24].

Table 6: Geometric and structural data.

Geometric parameters	Values	**Structural parameters**	Values
Aspect ratio	8.6	Density	2 780 kg/m^3
Taper ratio	0.3	Young modulus	73.1 GPa
Leading edge sweep	28.2°	Poisson ratio	0.33
Reference area	91 m^2	Shear correction factor	5/6
Airfoil	RAE 2822	Yield stress	324 MPa

Two scenarios are included in the optimization problem: a nominal cruise, and a $2.5g$ pull-up maneuver. The flight conditions are given in Table 7.

The objective of the optimization is to minimize the fuel burn W_{fuel} in cruise, which is computed

Table 7: Flight conditions.

Parameters	Symbols	Cruise	Maneuver
Load factor	n	1.0	2.5
Mach number	M_∞	0.82	0.78
Pressure altitude	h	35 000 ft	20 000 ft
Dynamic pressure	q_∞	11 250 Pa	19 850 Pa

using the Breguet formula,

$$W_{\text{fuel}} = (W_{\text{fixed}} + W_{\text{wing}}) \times \left(\exp\left(\frac{Rc_t}{V_\infty} \frac{C_{D_0} + C_D}{C_L} \right) - 1 \right), \tag{4}$$

where W_{fixed} is the fixed mass of the aircraft, W_{wing} is the mass of the structural wingbox, R is the mission range, c_t is the thrust specific fuel consumption, V_∞ is the true airspeed, and C_L is the lift coefficient. In order to account for the viscous drag, a fixed drag coefficient C_{D_0} is added to the drag coefficient C_D obtained using `DART`. The values of the different parameters have been derived from a typical cruise mission profile of an Embraer regional aircraft and are provided in Table 8.

Table 8: Cruise mission parameters for the RAE optimization case.

Parameters	Symbols	Values
Fixed weight	W_{fixed}	34 tons
Range	R	2 500 nm
Specific fuel consumption	c_t	0.65 h^{-1}
True airspeed	V_∞	473 kts
Fixed drag coefficient	C_{D_0}	0.022

Similar to the previous cases, the wing skin and the wingbox are embedded in a FFD box, whose points can move in the vertical direction to control the cross-sectional shape of the wing, as shown in Figure 4. Additionally, the twist angle of the last 3 sections along the wing span and the angle of attack of the freestream flow are allowed to change. Furthermore, the thickness of the 18 ribs, leading and trailing edge spars, 16 stringers and 324 skin panel patches are also used as design variables. The lift coefficient and the aircraft weight are related through the load factor n, which is constrained for the cruise and the maneuver conditions as

$$n = \frac{q_\infty S_{\text{ref}} C_L}{g\left(W_{\text{fixed}} + W_{\text{wing}} + \frac{W_{\text{fuel}}}{2}\right)} = \begin{cases} 1.0 & (\text{cruise}) \\ 2.5 & (\text{maneuver}) \end{cases}, \tag{5}$$

where q_∞ is the dynamic pressure, S_{ref} is the reference area and g is the acceleration due to gravity. Note that the trim Equation 5 does not account for any lifting surfaces other than the wing. The structural failure index of the wing is constrained to remain below a given threshold during the maneuver. The local failure criterion is computed in each shell element by dividing the von Mises stress by the yield stress, and the global index is calculated by aggregating the criterion over all the elements using a Kreisselmeier-Steinhauser function [26, 36]. The global failure index is multiplied by a safety factor of 1.5. The ratio of the internal volume of the wingbox to its initial value is constrained to be no less than the ratio of the fuel weight to its initial value, so that the fuel required for the flight can be stored inside the fuel tanks. This volume constraint is enforced from the wing root to 75% of the span, where the fuel tanks would be located in an actual wing. Furthermore, the height of the trailing edge spar is constrained to 80%

of its initial value, such that sufficient space is reserved for the attachment of the control surface actuation devices [35]. Similar to the previous cases, the leading edge radius and the trailing edge thickness are constrained to remain constant, and the upper and lower control points at the wing leading and trailing edges are constrained to move in equal and opposite direction. Finally, structural smoothness is ensured by constraining the difference in the thicknesses between adjacent structural elements to remain below a given value. The optimization tolerance is set to 1 kg and the different physics are coupled using a Block Gauss-Seidel scheme [37], whereby relative tolerances on the residuals for the direct and adjoint solutions are set to 10^{-6}. The optimization problem is summarized in Table 9.

Table 9: Summary of the RAE optimization problem.

Objective	Number of variables	Bounds	Scaling
Fuel burn	1	–	10^{-4}
Design variables			
Fuel available fraction	1	$[0.5; 1.5]$	1
Angle of attack	1	$[0; 5]^\circ$	1
Shape	70	$[-10; 10]$ cm	10^1
Twist	3	$[-5; 5]^\circ$	1
Ribs thickness	18	$[1; 20]$ mm	10^2
Spar thickness	36	$[1; 20]$ mm	10^2
Stringers thickness	288	$[1; 20]$ mm	10^2
Skin thickness	324	$[1; 20]$ mm	10^2
Nonlinear constraints			
Trim	2	$= 1$	1
Failure	1	$= 1/1.5$	1.5
Fuel fraction	1	$[100; -]$ %	1
Wing volume ratio	1	$[100; -]$ %	1
Leading edge radius	10	$[100; -]$ %	1
Trailing edge thickness	10	$[100; -]$ %	1
Trailing edge spar height	10	$[80; -]$ %	1
Linear constraints			
Leading/trailing edge	10	$= 0$ m	1
Structural smoothness	1 256	$[-; 1]$ mm	10^3

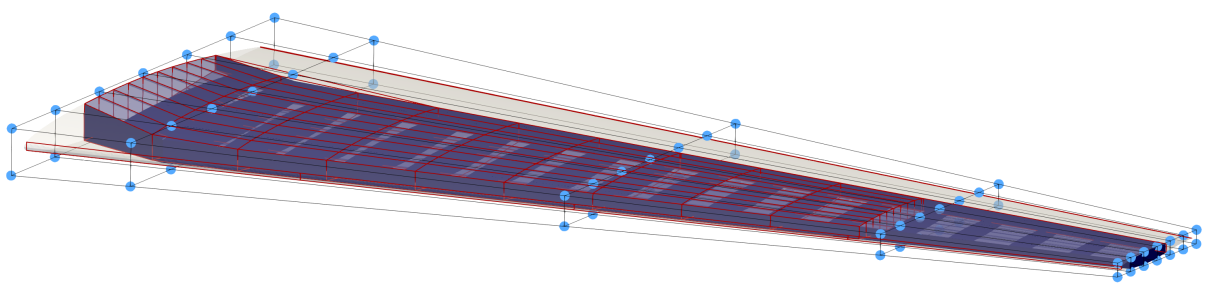

Figure 4: Optimization setup for the RAE wing case. The aerodynamic and geometric design variables are indicated in light blue and the geometric constraints are displayed in dark blue.

3.2.1 Grid convergence

As in the previous cases, the aerodynamic computation is performed in a domain discretized using tetrahedral elements. A grid convergence analysis is carried out at $2.55°$ angle of attack and Mach $M_\infty = 0.82$. All computations converged in nine coupling iterations. The results provided in Table 10 indicate that the medium mesh yields sufficiently converged results. Note that only the inviscid drag contribution is shown.

Table 10: Cell count, aerodynamic coefficients, tip displacements and computational times obtained using three grids for the RAE case.

Mesh	N. cells	C_L	C_D	Δ_{tip}	CPU time
Coarse	330 978	0.3830	0.00802	1.18 m	5.4 min
Medium	655 569	0.4069	0.00931	1.22 m	12.8 min
Fine	1 118 925	0.4080	0.00996	1.24 m	21.4 min

3.2.2 Optimization convergence and computational time

The optimization computation is started from two different initial conditions, a light and a heavy structural wingbox weight, by setting the thickness of all the structural patches to a uniform value. The path taken by the optimization process, illustrated as a function of the wingbox weight and the aircraft lift-to-drag ratio, and by the evolution of the load factors, the failure criterion and the fuel burn as a function of the iterations are depicted in Figure 5. The light case required 50 functional evaluations to converge, while the heavy case converged in 39 iterations. Although the optimized designs differ, the two cases follow a similar pattern, whereby both the structural weight and the lift-to-drag-ratio increase, and achieve a similar reduction in fuel burn. A more realistic case would consist in using a pre-optimized wing as an initial condition, whereby the wingbox would have been designed using maneuver loads obtained on a rigid geometry.

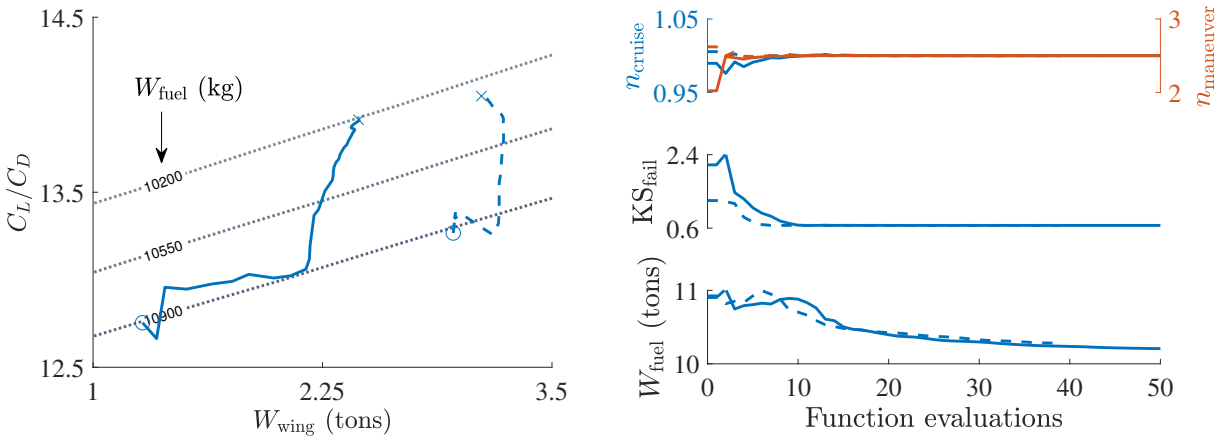

(a) Fuel burn as a function of structural wingbox mass and lift-to-drag ratio.

(b) Load factors, failure criterion and fuel burn as a function of iteration count.

Figure 5: Path and history of the RAE optimization cases. Blue: cruise, red: maneuver. Solid: light, dashed: heavy.

The computations were run in serial and parallel on a desktop workstation equipped with an AMD 3970X processor rated at 3.7 GHz. Message Passing Interface (MPI) has been used to

distribute the computation of the scenarios, while multi-threading has been used to run DART in parallel. The number of gradient and functional evaluations, as well as the computational time are given in Table 11. The wall-clock time is less than twenty-four hours for both the light and heavy cases. Although running the scenarios and DART in parallel reduces the computational cost, the scaling is quite poor. Firstly, MPI scales roughly as 1.3 out of 2. This is because each scenario requires a different number of aerostructural coupling iterations to converge, and the two scenarios need to be converged before the gradients can be computed. Secondly, the scaling factor due to multi-threading is roughly of 1.4 out of 4. This is mainly due to the linear solver used in DART, whose scaling factor is typically around 0.5. Furthermore, only DART, which requires about 75% of the computational time, is run in parallel, while TACS and MELD are run in serial.

Table 11: Number of gradient and functional evaluations, and computational time required for the RAE cases. n is the number of MPI processes and k is the number of threads per process.

	Light		Heavy	
$\mathbf{n \times k}$	N. grad./func. eval.	Wall-clock time	N. grad./func. eval.	Wall-clock time
1×1	$49/50$	23.0 h	$37/39$	19.3 h
1×4	$49/50$	16.8 h	$37/39$	13.6 h
2×1	$49/50$	17.9 h	$37/39$	15.4 h
2×4	$49/50$	13.7 h	$37/39$	11.1 h

3.2.3 Lift and pressure coefficients

The sectional lift coefficient distributions along the span of the baseline and optimized RAE wing obtained in cruise and maneuver conditions are illustrated in Figure 6. For conciseness, only the light case is considered in the next analyses. The optimization process adapted the twist of the wing so that the loads are shifted inboard. This has two advantages. Firstly, the optimized lift distributions are closer to the elliptical lift distribution, which reduces the induced drag. Secondly, the bending moment at the root is reduced, which in turn reduces the deflection at the wingtip.

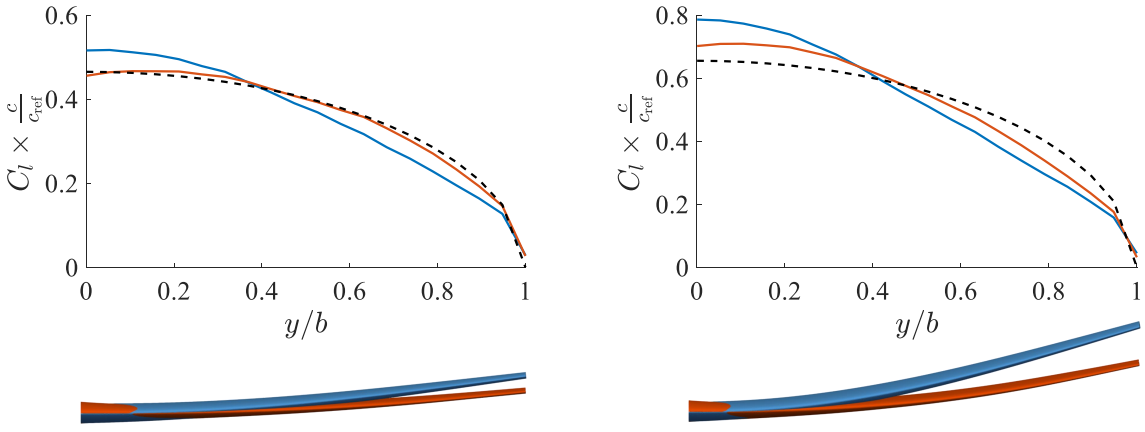

(a) Cruise ($M_\infty = 0.82$ at 35 000 ft). (b) Maneuver ($M_\infty = 0.78$ at 20 000 ft).

Figure 6: Sectional lift coefficient distribution along the span of the baseline and optimized RAE wing, in cruise and maneuver conditions. Black dashed: elliptical distribution, blue: baseline, red: optimized.

The pressure coefficient contour on the suction side of the baseline and optimized RAE wing obtained in cruise condition is depicted in Figure 7. Additionally, the pressure coefficients are extracted along the chord at four spanwise stations and plotted in Figure 8. Note that the station located at 41% semi-span corresponds to the mean aerodynamic chord position. Overall, the optimization process adapted the original RAE 2822 airfoil in order to suppress the strong shock on the suction side of the wing, which allowed to reduce the drag while increasing the lift. As in the NACA and Onera cases, the optimization produced some bumps on the wing's surface. While these bumps are small on the inboard section of the wing, their amplitudes become bigger outboard. Resorting to viscous-inviscid interaction or improving the thickness constraints might help alleviate this issue.

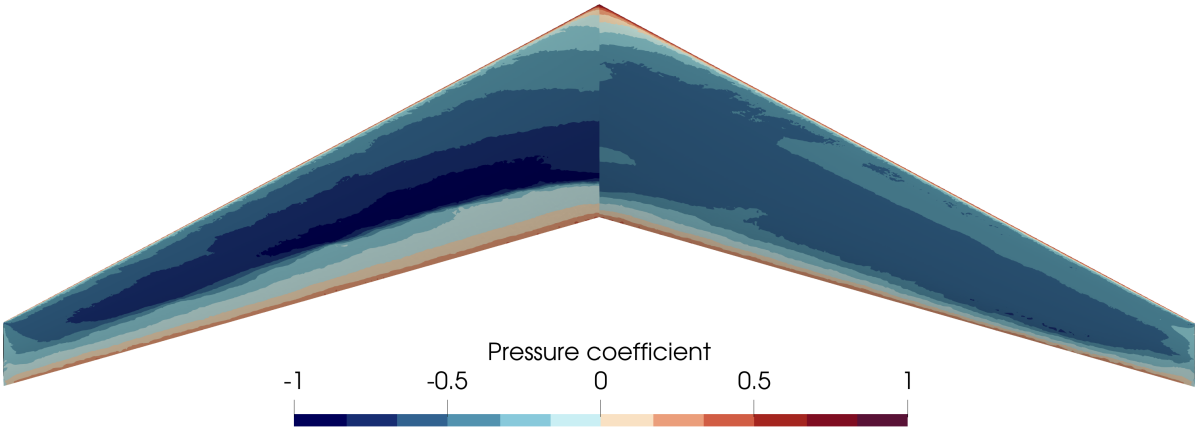

Figure 7: Pressure coefficient contour on the suction side of the baseline (left) and optimized (right) RAE wing in cruise ($M_\infty = 0.82$ at 35 000 ft).

3.2.4 Structural thickness and failure criterion

The thickness of the structural patches and the failure criterion computed on the baseline and optimized RAE wing in maneuver are shown in Figure 9. The thickness of the ribs has decreased to about 1 mm. Moreover, the thickness of the other structural components has been tailored to the loads: it increased inboard, and remained small at the wingtip. This modification decreased the failure index below the imposed threshold, particularly on the inboard section, where it was initially violated.

4 CONCLUSION

In the present work, the discrete adjoint full potential code `DART`, has been integrated in a state-of-the-art multi-disciplinary analysis and optimization framework in order to perform aerostructual computations for preliminary aircraft design. The code is based on finite elements and is open-source. The methodology has been demonstrated by means of aerodynamic and aerostructural optimization calculations performed on typical wings. Overall, the adjoint full potential formulation allows to design optimized wing shapes and structures at low computational cost, regardless of the number of design variables, which is of paramount importance in the preliminary design stage. More specifically, the optimizer produces supercritical airfoils adapted to the transonic conditions, so that shocks are suppressed and wave drag is reduced. Moreover, the twist along the wing span is adapted such that the tip vortices and the induced drag are reduced. Finally, the thickness of structural components is tailored to the loads, which allows to design a light wing respecting the failure criterion of the material. A typical aerostructural

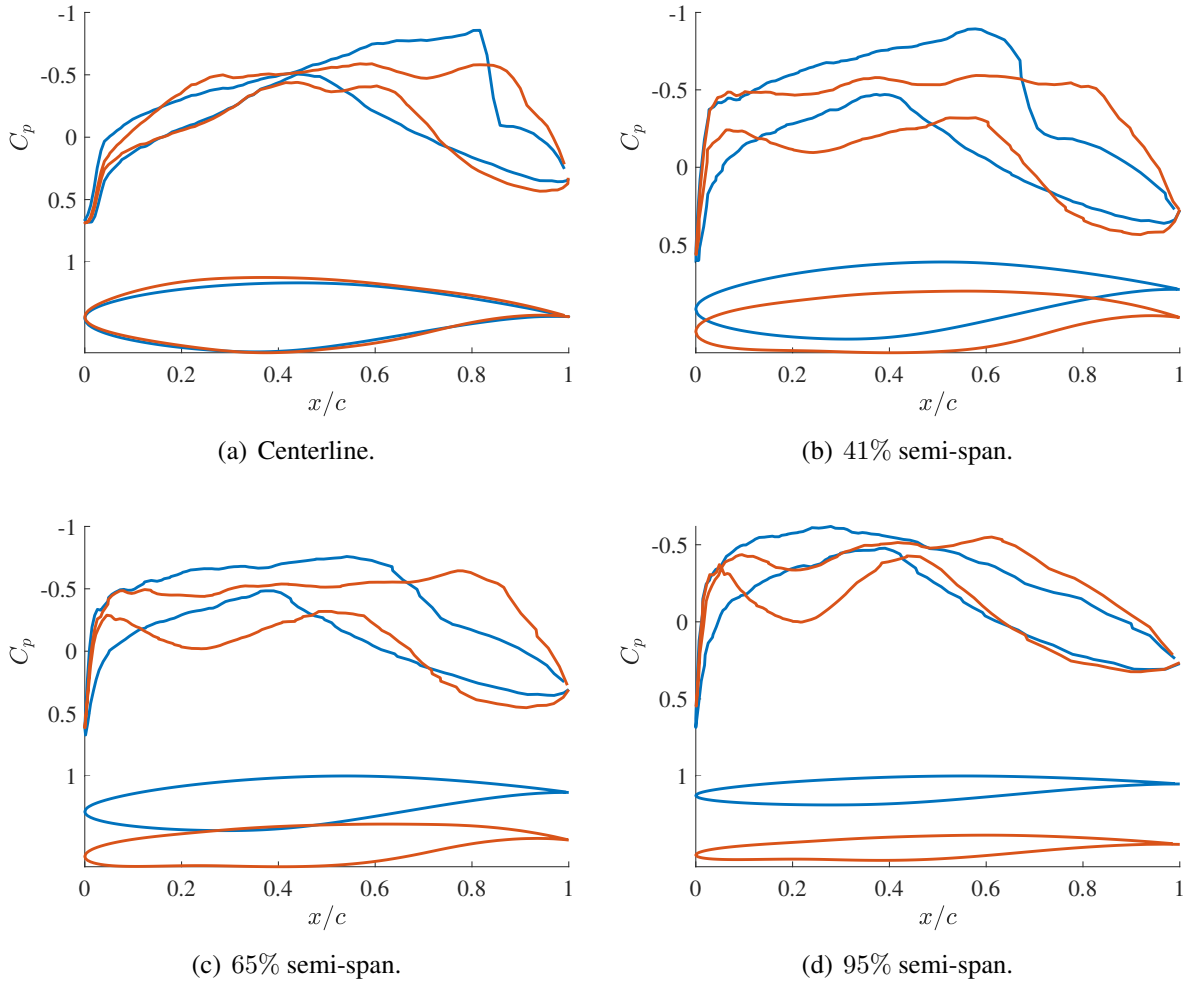

(a) Centerline.

(b) 41% semi-span.

(c) 65% semi-span.

(d) 95% semi-span.

Figure 8: Pressure coefficient computed on the baseline and optimized geometry of the RAE wing in cruise ($M_\infty = 0.82$ at 35 000 ft). Blue: baseline, red: optimized.

optimization computation takes less than a day on a single core of a modern computer workstation. The computational time can be further reduced to half a day by using both shared and distributed memory parallelization. The next steps consist in improving the formulation of the optimization problem. More specifically, a structural wingbox designed using loads obtained on a rigid wing will be used as an initial condition. Buckling constraints will also be considered. Additionally, the planform shape will be parametrized so that the taper ratio, the sweep and the dihedral angles can be optimized as well. Finally, the aerodynamic, the structural and the geometric models will be improved. A viscous-inviscid interaction method will be implemented to account for viscous effects. A more detailed structural model, made of composite material and including non-aerodynamic loads such as fuel loads, will be considered. Ultimately, the methodology will be applied to full aircraft configurations, and results will be compared to higher-fidelity computations.

5 ACKNOWLEDGMENT

The authors gratefully thank Anil Yildirim (University of Michigan), Kevin Jacobson (NASA Langley Research Center) and Justin Gray (NASA Glenn Research Center) for granting early access to the software `MPHYS`. The authors would also like to thank Luc Papeleux (University of Liège) for his precious help. The authors would finally like to acknowledge the aerospace com-

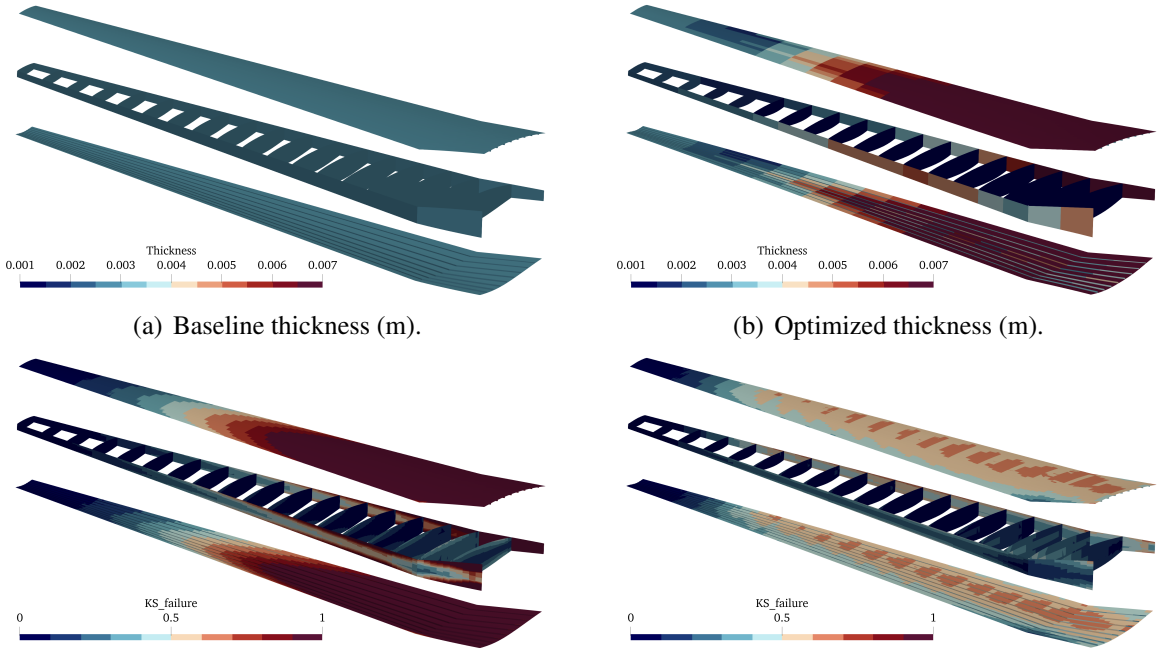

(a) Baseline thickness (m).

(b) Optimized thickness (m).

(c) Baseline failure criterion.

(d) Optimized failure criterion.

Figure 9: Thickness and failure criterion of the baseline and optimized structural wingbox for the RAE wing in maneuver ($M_\infty = 0.78$ at 20 000 ft).

pany Embraer S.A. for partly funding the present work, the MDO Lab members for providing the structural model of the RAE benchmark, and the Consortium des Équipements de Calculs Intensifs (CÉCI), funded by the Fonds de la Recherche Scientifique de Belgique under Grant No. 2.5020.11, for providing the computational resources that helped to develop and validate `DART`.

6 REFERENCES

[1] Shirk, M. H. and Hertz, T. J. (1986). Aeroelastic Tailoring - Theory, Practise and Promise. *Journal of Aircraft*, 23(1), 6–18.

[2] Mura, G. L. (2017). *Mesh Sensitivity Investigation in the Discrete Adjoint Framework*. Ph.D. thesis, University of Sheffield.

[3] Yu, Y., Lyu, Z., Xu, Z., et al. (2018). On the influence of optimization algorithm and initial design on wing aerodynamic shape optimization. *Aerospace Science and Technology*, 75, 183–199. ISSN 1270-9638. doi:https://doi.org/10.1016/j.ast.2018.01.016.

[4] Martins, J. R. R. A. and Hwang, J. T. (2013). Review and Unification of Methods for Computing Derivatives of Multidisciplinary Computational Models. *AIAA Journal*, 51(11), 2582–2599.

[5] Hwang, J. T. and Martins, J. R. R. A. (2018). A computational architecture for coupling heterogeneous numerical models and computing coupled derivatives. *ACM Transactions on Mathematical Software*, 44(4), Article 37.

[6] Martins, J., Alonso, J., and Reuther, J. (2005). A Coupled-Adjoint Sensitivity Analysis Method for High-Fidelity Aero-Structural Design. *Optimization and Engineering*, 6(1), 33–62. ISSN 1573-2924. doi:https://doi.org/10.1023/B:OPTE.0000048536.47956.62.

[7] Sanchez, R., Albring, T., Palacios, R., et al. (2018). Coupled adjoint-based sensitivities in large-displacement fluid-structure interaction using algorithmic differentiation. *International Journal for Numerical Methods in Engineering*, 113(7), 1081–1107. doi: https://doi.org/10.1002/nme.5700.

[8] Kenway, G. K., Mader, C. A., He, P., et al. (2019). Effective adjoint approaches for computational fluid dynamics. *Progress in Aerospace Sciences*, 110, 100542. ISSN 0376-0421. doi:https://doi.org/10.1016/j.paerosci.2019.05.002.

[9] Wright, J. R. and Cooper, J. E. (2015). *Static Aeroelasticity and Flutter*, chap. 22. John Wiley and Sons, pp. 475–480.

[10] Crovato, A., Almeida, H. S., Vio, G., et al. (2020). Effect of Levels of Fidelity on Steady Aerodynamic and Static Aeroelastic Computations. *Aerospace*, 7(4), 42. doi:https://doi.org/10.3390/aerospace7040042.

[11] Crovato, A. (2020). *Steady Transonic Aerodynamic and Aeroelastic Modeling for Preliminary Aircraft Design*. Ph.D. thesis, University of Liège.

[12] Crovato, A., Prado, A. P., Cabral, P. H., et al. (2022). An adjoint full potential solver for fast aerostructural optimization in preliminary aircraft design. *Submitted to Aerospace Science and Technology*.

[13] Farhat, C., Lesoinne, M., and Maman, N. (1995). Mixed explicit/implicit time integration of coupled aeroelastic problems: Three-field formulation, geometric conservation and distributed solution. *International Journal for Numerical Methods in Fluids*, 21(10), 807–835. doi:https://doi.org/10.1002/fld.1650211004.

[14] Maute, K., Nikbay, M., and Farhat, C. (2003). Sensitivity analysis and design optimization of three-dimensional non-linear aeroelastic systems by the adjoint method. *International Journal for Numerical Methods in Engineering*, 56(6), 911–933. doi:https://doi.org/10.1002/nme.599.

[15] Gray, J. S., Hwang, J. T., Martins, J. R. R. A., et al. (2019). OpenMDAO: An open-source framework for multidisciplinary design, analysis, and optimization. *Structural and Multidisciplinary Optimization*, 59(4), 1075–1104.

[16] Kraft, D. (1988). *A software package for sequential quadratic programming*. Deutsche Forschungs- und Versuchsanstalt für Luft- und Raumfahrt Köln: Forschungsbericht. Wiss. Berichtswesen d. DFVLR.

[17] Nocedal, J. and Stephen, J. W. (2006). *Sequential Quadratic Programming*. New York, NY: Springer New York. ISBN 978-0-387-40065-5, pp. 529–562.

[18] Wu, N., Kenway, G., Mader, C. A., et al. (2020). pyOptSparse: A Python framework for large-scale constrained nonlinear optimization of sparse systems. *Journal of Open Source Software*, 5(54), 2564. doi:10.21105/joss.02564.

[19] Kenway, G. K. W., Kennedy, G. J., and Martins, J. R. R. A. (2010). A CAD-Free Approach to High-Fidelity Aerostructural Optimization. In *Proceedings of the 13th AIAA/ISSMO Multidisciplinary Analysis Optimization Conference*. Fort Worth, TX. AIAA 2010-9231.

[20] Sederberg, T. W. and Parry, S. R. (1986). Free-form deformation of solid geometric models. *SIGGRAPH Computer Graphics*, 20(4), 151–160. ISSN 0097-8930. doi: 10.1145/15886.15903.

[21] Dwight, R. P. (2009). Robust Mesh Deformation using the Linear Elasticity Equations. *Journal of Computational Fluid Dynamics*, 12, 401–406.

[22] Widhalm, M., Brezillon, J., Ilic, C., et al. (2010). Investigation on adjoint based gradient computations for realistic 3d aero-optimization. In *Proceedings of the 13th AIAA/ISSMO Multidisciplinary Analysis Optimization Conference*. doi:10.2514/6.2010-9129.

[23] Geuzaine, C. and Remacle, J.-F. (2009). Gmsh: a three-dimensional finite element mesh generator with built-in pre- and post-processing facilities. *International Journal for Numerical Methods in Engineering*, 79, 1309–1331.

[24] Kennedy, G. J. (2014). A parallel finite-element framework for large-scale gradient-based design optimization of high-performance structures. *Finite Elements in Analysis and Design*, 87, 56–73. ISSN 0168-874X.

[25] Kennedy, G. J. (2015). Strategies for adaptive optimization with aggregation constraints using interior-point methods. *Computers and Structures*, 153, 217–229. ISSN 0045-7949.

[26] Kennedy, G. J. and Hicken, J. E. (2015). Improved constraint-aggregation methods. *Computer Methods in Applied Mechanics and Engineering*, 289, 332–354. ISSN 0045-7825.

[27] Boopathy, K. and Kennedy, G. J. (2019). Parallel Finite Element Framework for Rotorcraft Multibody Dynamics and Discrete Adjoint Sensitivities. *AIAA Journal*, 57(8), 3159–3172.

[28] Kiviaho, J. F. and Kennedy, G. J. (2019). Efficient and Robust Load and Displacement Transfer Scheme Using Weighted Least Squares. *AIAA Journal*, 57(5), 2237–2243.

[29] Schmitt, V. and Charpin, F. (1979). Pressure distributions on the ONERA-M6-wing at transonic Mach numbers. *Experimental data base for computer program assessment*, 4.

[30] Brooks, T. R., Kenway, G. K. W., and Martins, J. R. R. A. (2018). Benchmark Aerostructural Models for the Study of Transonic Aircraft Wings. *AIAA Journal*, 56(7), 2840–2855.

[31] Drela, M. and Giles, M. (1987). Viscous-Inviscid Analysis of Transonic and Low Reynolds Number Airfoils. *AIAA Journal*, 25(10), 1347–1355.

[32] Bilocq, A. (2020). *Implementation of a viscous-inviscid interaction scheme in a finite element full potential solver*. Master's thesis, University of Liège.

[33] Dechamps, P. (2022). *Improvement of the viscous-inviscid interaction method implemented in DARTFlo*. Master's thesis, University of Liège.

[34] Lyu, Z., Kenway, G. K., Paige, C., et al. (2013). Automatic Differentiation Adjoint of the Reynolds-Averaged Navier-Stokes Equations with a Turbulence Model. In *21st AIAA Computational Fluid Dynamics Conference*. doi:10.2514/6.2013-2581.

[35] Kenway, G. K. and Martins, J. R. R. A. (2014). Multi-point High-fidelity Aerostructural optimization of a Transport Aircraft Configuration. *Journal of Aircraft*, 51(1), 144–160.

[36] Kreisselmeier, G. and Steinhauser, R. (1979). Systematische Auslegung von Reglern durch Optimierung eines vektoriellen Gütekriteriums. *Automatisierungstechnik*, 27(1-12), 76–79.

[37] Wood, C., Gil, A. J., Hassan, O., et al. (2010). Partitioned Block-Gauss–Seidel coupling for dynamic fluid–structure interaction. *Computers and Structures*, 88(23), 1367–1382.

COPYRIGHT STATEMENT